In the format provided by the authors and unedited.

On Phonons and Water Flow Enhancement in Carbon Nanotubes

Eduardo R. Cruz-Chú, Ermioni Papadopoulou, Aleksandar Popadić, Gengyun Li,

Jens H. Walther, Matej Praprotnik, Petros Koumoutsakos

This Supplementary Information includes details of the simulation set-up and protocols, theoretical derivations and further results not included in the manuscript due to shortage of space but crucial to the findings of this study. The Supplementary Information consists of the following sections:

S1   Methods

Computational Setup

We study, via Molecular Dynamics (MD) simulations, double-walled carbon nanotubes (CNTs) filled with water. The CNTs have chiral indexes of (20,20) and (25,25) and we consider periodic domains with axial lengths of 15 nm, 20 nm, and 30 nm. The outer CNTs remain rigid while three different settings are employed for the *inner* CNT atoms: phonon-active, phonon-free and fixed cases. Phonon-active and phonon-free cases are defined in Ma *et al.* [4] as follows: phonon-active case, with CNT vibrations determined by bonding potentials (bonds, angles, dihedrals); and phonon-free case, with phonon modes canceled by removing bonding terms. For the latter case, CNT vibrations are determined through positional harmonic constraints, which provide a restoring force each time the CNT atoms move from their original positions. The harmonic constants are set to the following values: 23.06 kcal mol^{-1}Å^{-2} (1κ), 46.12 kcal mol^{-1}Å^{-2} (2κ), and 230.6 kcal mol^{-1}Å^{-2} (10κ). The additional fixed case considers all CNT atoms rigid.

We have built all the atomistic models used in this study by developing a TCL-package tool, named WCCNT (Water Confinement in Carbon Nanotubes) [8]. The WCCNT works within the VMD software interface [9] as a TCL plugin, and it integrates different routines to generate and analyze LAMMPS-compatible files of CNTs with water. We build CNTs with armchair chiralities of (20,20) and (25,25) and lengths of 15, 20, and 30 nm. In the following, (20,20) and (25,25) CNTs are referred to as inner and outer CNTs, respectively. Inner and outer CNTs of similar lengths are arranged in concentric double-walled CNT configuration (DWNT).

In order to solvate the DWNT pores, we proceed as follows: nine DWNTs are arranged in a grid of 3×3 with a grid spacing of 7.5 nm (Figure S1a). The DWNT grids are immersed in a rectangular water box of 30 nm side. We ensure that no water molecules exist between the inner and outer CNTs, by removing initially all water molecules within a distance of 0.5 nm from the carbon atoms. Then, the systems are equilibrated using MD in the isothermal-isobaric (NPT) ensemble (see below for details) for 1 ns, while all carbon atoms remain fixed. This equilibration results in constant water density inside DWNTs (Figures S1b and S1c). The average water density over the last frames is 1.094 ± 0.003 gr cm^{-3}, assuming an effective internal radius of 1.1 nm (Figure S1b). After solvation, the atomistic coordinates of the DWNTs filled with water are used as starting point for further simulations. Each system is placed in a periodic box of 10×10×L nm^3, where L is the CNT axial length (15, 20, or 30 nm).
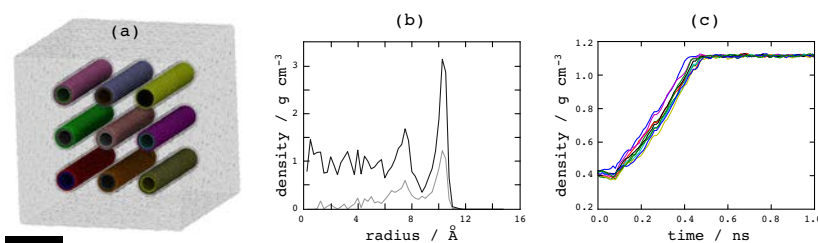
Figure S1: Solvation of DWNT systems. (a) The snapshot shows the initial configuration of DWNT with 9 copies of a 20-nm length CNT in a solvation box. The system is MD simulated to reach constant water density inside the lumen of DWNT. CNTs are shown in different colors, water box as a Gray box. Scale bar is 10 nm. (b) Radial density profile for one of the 9 nanotube systems at initial configuration (gray line) and after 10 ns (black line). Density close to the pore center approaches water bulk density (1 *gr cm^{-3}*). (c) Water permeation. The plot shows 9 colored curves, each color representing the permeation of one DWNT in a 3×3 grid. Note that water density converges to a constant value after 0.5 ns.

Three different settings are applied to the inner CNT atoms: (a) phonon-active CNT: two rings of CNT atoms are fixed at the periodic ends, while the rest of CNT atoms are allowed to move, (b) phonon-free CNT: bonding terms are removed (bond, angle, and dihedral potential terms), CNT atoms are restrained to their initial position by harmonic oscillators, (c) fixed CNT: all carbon atoms are kept rigid. For the phonon-free case, three spring constants are used: 23.06 Kcal mol^{-1}Å^{-2} (1κ), 46.12 Kcal mol^{-1}Å^{-2} (2κ), and 230.6 Kcal mol^{-1}Å^{-2} (10κ). In all cases the outer CNTs are fixed. All nine systems, under five CNT settings (1 phonon-active, 3 phonon-free, 1 fixed), are equilibrated for 1 ns in the canonical (NVT) ensemble with the water and mobile carbons kept at 298 K. The last configurations are used for the production runs.

Molecular Dynamics (MD) Simulation Protocol

All MD simulations are performed with the MD package LAMMPS [1] using 1 fs timestep and periodic boundary conditions. We use the TIP4P-Ew water model [2] with molecular geometry constrained by the SHAKE algorithm [3], and the CNT force field employed by Ma *et al.* [4], which combines bonding terms from the Dreiding force field [5] with a fine-tuned Lennard-Jones potential that produces a water contact angle of 54.4°. We remark that such a contact angle enhances the interactions between the CNT atoms and their phonons and the water molecules, but implies rather hydrophilic behavior for the CNTs. For short range interactions, we use a cutoff of 1.2 nm; for long-range electrostatic interactions, we use a particle-particle particle-mesh (P3M) algorithm [6] with a root-mean-squared error in the force calculation of 10^{-5}, unless otherwise stated (see section S7). Simulations are carried out in three ensembles: microcanonical (NVE), canonical (NVT) at 298 K, and isothermal-isobaric (NPT) at 298 K and 1 atm; temperature and pressure are controlled using the Nosé-Hoover method [7].

In Ma *et al.* [4], a novel approach was introduced to harness computer resources to study water flow in CNTs. They used distributed computing resources to increase the statistical sampling space, performing 5 million short MD simulations. Similar small-system massive-sampling approaches are currently used for protein folding studies [10] as well as in quantifying safe parameter-regions of MD models [11, 12, 13]. We followed this protocol using Π4U [14] propagation step; as MD simulations are independent, they can be automatically submitted for asynchronous execution as tasks.

Two groups of simulations are initially performed in the present study. We hereby name the first set, corresponding to force driven calculations, as *FLOW* and the not-force-driven simulations for diffusion estimation as *DIFF*. For both groups, the mobile inner CNT atoms are kept at 298 K and the water molecules are not thermostated. Similar protocols were used in the study by Ma *et al.*.

In the group of force-driven simulations, a single phonon CNT system is equilibrated for 10 ps, then the flow rate set to zero, and finally a force of 0.012 pN is applied to each water oxygen for 10 ps (Figure S3-black line). 650 thousand samples of such system are simulated, using different seed numbers to initialize velocity distributions. The total computational effort for the force-driven simulation group is estimated: 650000 simulations × 0.020 ns each MD simulation = **13 μs**.

In the group of not-force-driven simulations, water molecules diffuse freely without the influence of any external force for at least 10 ns. The total computational effort for this simulation group is: ([9 systems × 3 CNT cases (fixed, phonon-active and phonon-free 1κ)] + [5 systems × 2 CNT cases (phonon-free 2κ and 10κ)]) × 10 ns each MD simulation = **370 ns**. We perform an extra test for diffusion using phonon CNTs of different lengths: for 15-nm long CNT, nine systems, for each MD simulation the last 10 ns is kept; for 30-nm long CNT, nine systems, each MD simulation last 10 ns. The computational effort for extra diffusion test being (9 systems of 15-nm CNT × 10 ns each MD simulation) + (9 systems of 30-nm CNT × 10 ns each MD simulation) = **180 ns**.

To evaluate effects that lead to diffusion variation in CNTs, we performed two more groups of simulations, so-called Heat Transfer (*HEAT*) and Friction Coefficient (*FRIC*). In group for heat transfer simulations, we tested four CNT settings (phonon-active, phonon-free with three spring constants).

First, the systems are equilibrated in NVT ensemble for 1 ns, water and CNT are thermostated. After that, we perform production runs as follows: 8-ns MD equilibration, only inner CNTs are thermostated, while an axial force of 0.012 pN is applied to oxygen atoms. Such force is needed to accelerate the flow and generate a measurable heat transfer between water and CNT. The computational effort for the group of Heat transfer simulations is: 4 CNT cases × 3 systems for each CNT case × 8 ns = **96 ns**. For the group for friction evaluation, the starting configurations are the last frames of the not-force-driven group. The production runs consist of 0.5 ns MD simulations, using five different CNT cases (fixed, phonon-active, phonon-free with three spring constants). For each CNT case, 5 systems are simulated. Total forces between water and carbon are saved every timestep (1 fs) for time correlation analysis (see Section S8). The computational effort for the group for friction evaluation is: 5 CNT cases × 5 systems for each CNT case × 0.5 ns each MD simulation = **12.5 ns**.

MD simulations are summarized in Table S1. This table does not include pre-production MD equilibrations nor MD simulations used to study the effects of the MD protocol parameters on water heating (Section S7).

Label	CNT setting	Force	Length [nm]	Therm. Water	Time	Num. MD Sim.	Group
1	Phonon	**Yes**	20	No	20 ps	6.5×10^5	FLOW
2	Fixed	**Yes**	20	No	20 ps	5×10^4	FLOW
3	Fixed	No	20	No	10 ns	9	DIFF
4	Phonon-Active	No	20	No	10 ns	9	DIFF
5	Phonon-Free-1κ	No	20	No	10 ns	9	DIFF
6	Phonon-Free-2κ	No	20	No	10 ns	5	DIFF
7	Phonon-Free-10κ	No	20	No	10 ns	5	DIFF
9	Phonon-Active	No	**15**	No	10 ns	9	DIFF
10	Phonon-Active	No	**30**	No	10 ns	9	DIFF
11	Phonon-Active	**Yes**	20	No	8 ns	3	HEAT
12	Phonon-Free-1κ	**Yes**	20	No	8 ns	3	HEAT
13	Phonon-Free-2κ	**Yes**	20	No	8 ns	3	HEAT
14	Phonon-Free-10κ	**Yes**	20	No	8 ns	3	HEAT
15	Fixed	No	20	**Yes**	0.5 ns	5	FRIC
16	Phonon-Active	No	20	**Yes**	0.5 ns	5	FRIC
17	Phonon-Free-1κ	No	20	**Yes**	0.5 ns	5	FRIC
18	Phonon-Free-5κ	No	20	**Yes**	0.5 ns	5	FRIC
19	Phonon-Free-10κ	No	20	**Yes**	0.5 ns	5	FRIC

Table S1: MD simulation campaign for periodic DWNTs.

S2   Force-driven simulations for shear-stress calculation

Oscillations in shear stress

For force-driven simulations, *FLOW*, as defined in Section S1, we observe an oscillatory pattern of τ similar to that observed in Ma *et al.* [4]. The force on water molecules induces a linear, axial velocity (ν) of the water Center-of-Mass (CoM) with small-amplitude oscillations (Figure S2a). The frequency of these oscillations correlates well with the axial CoM velocity of the CNT, ν_{CNT} (Figure S2c), confirming that ν oscillations stem from axial CNT phonon modes. The shear-stress is calculated as $\tau \sim \dot{\nu}$ (see below); thus, any non-linear perturbation of ν is reflected in τ (Figure S2b). In MD-simulations with fixed CNTs, the oscillatory behavior of ν disappears. However, the overall water accelerations for phonon-active and fixed CNTs are equal (Figure S2d), indicating independence of diffusion enhancement and CNT vibrations.
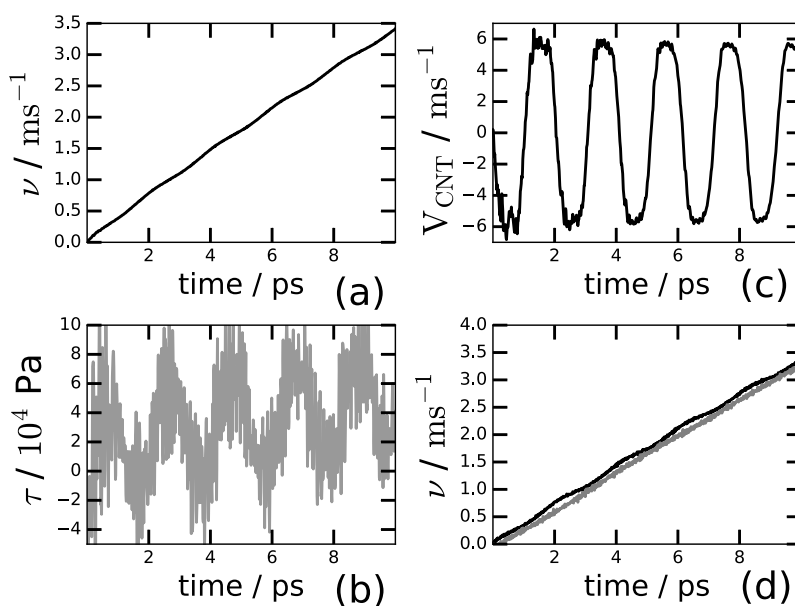
Figure S2: Water transport through phonon-active CNTs. (a) Axial CoM velocity for water ν, (b) water shear stress τ, and (c) axial CoM velocity for inner CNT V_{cnt} as a function of time. Panels (a), (b), and (c) show average quantities over 650 thousand force-driven simulations using a CNT of 20 nm length. Panel (d) shows a comparison of ν using phonon-active and fixed CNTs; curves show average quantities over 25 thousand samples. Flow acceleration computed as the slope of the curve is 0.337×10^{12} m s^{-2} and 0.335×10^{12} m s^{-2} for phonon-active and fixed CNTs, respectively.

Effect of magnitude of axial force

In their initial study, Ma *et al.* [4] applied force distributed between hydrogen and oxygen atoms equal to 0.012 pN. We tested that case (Figure S3-red line), as well as a case with a force of 0.024 pN applied to the oxygen atoms (Figure S3-blue line). In all three cases, the velocity scales linearly with time, whereas the period of the oscillations remains unaltered.
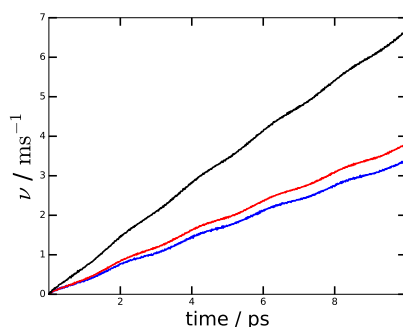
Figure S3: Effect of pulling force on water velocity. The plot compares the water velocity obtained by applying a force of 0.012 pN to oxygen atoms (black line), 0.012 pN distributed between hydrogen atoms (blue line), and 0.024 pN to oxygen atoms (red line). Note that the period of the oscillations does not change. The black, blue and red lines represent averages over 650 thousand, 250 thousand, and 500 thousand samples, respectively.

Shear stress from axial velocity

To calculate shear-stress (τ) from force-driven simulations, we employed the approach introduced by M. Ma *et al.* [4], where τ is computed from the force balance:

$$F = \tau A + Ma, \tag{1}$$

where F is the external force applied to the fluid, A is the area of the inner CNT, M is the total mass of water, and a is the flow acceleration. That is, F acts on water to overcome τ and accelerate the flow. Thus:

$$\tau = \frac{F - Ma}{A}, \tag{2}$$

A is computed using an inner radius of 1.35 nm. Note that F, M, and A are constants, and the only varying quantity is a. Thus, Equation 2 can be written as:

$$\begin{aligned} \tau &= \mathrm{G} + \mathrm{H}a \\ \tau &\sim a \end{aligned} \tag{3}$$

where G and H are constants, and τ is only affected by a. In turn, a is computed from the axial CoM velocity of water (nu) as:

$$a(t) = \frac{\nu(t + \Delta t) - \nu(t + \Delta t)}{2\Delta t} \tag{4}$$

therefore:

$$\tau \sim \dot{\nu} \tag{5}$$

In this way, any non-linear perturbation of ν is translated into a perturbation of τ, and as ν oscillates, τ responds in a similar fashion.

To validate our simulations against Ma *et al.*'s results [4], we compute a linear relationship without oscillations between τ and ν. We subtract the axial CoM velocity of the inner CNT (V_{cnt}) from the axial CoM velocity of the flow (ν). Figure S4 reveals a scatter plot, resembling a previously reported result [4], the slope being 0.47×10^4 MPa s m^{-1}. The previously reported slopes are 0.6×10^4 MPa s m^{-1} [4] and 0.49×10^4 MPa s m^{-1} [15].
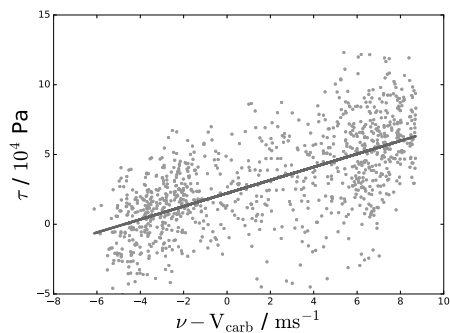
Figure S4: Linear relationship between shear stress and water velocity. By subtracting this periodic oscillation from τ [4], the theoretically expected linear response between τ and ν is recovered. The plot shows average values over 650 thousand MD simulations.

S3   Sensitivity analysis of axial velocity and shear-stress with number of samples

The short time scale of the force-driven simulations (10 ps) demands intensive averaging to visualize the subtle oscillations in τ and ν. In their initial work, Ma *et al.* (Supp. Inf. in [4]) estimated the number of samples needed (N) to obtain an observable τ from:

$$\Delta\tau = \frac{\Delta\tau_O}{\sqrt{N}} \tag{6}$$

where $\Delta\tau$ is the standard deviation of τ, and $\Delta\tau_O$ is 1.446 MPa. As the amplitude of τ is very small, τ oscillations are hidden by averaged fluctuations ($\Delta\tau$). Thus, very high N values are needed to significantly reduce $\Delta\tau$ and obtain a clear oscillating τ pattern. Based on this analysis, an oscillating τ is indeed observable within 500 thousand samples, as the estimated $\Delta\tau$ for N=500000 is 2.04 kPa; namely 5% of a 40 kPa τ amplitude. Our simulations confirm the emergence of an oscillatory τ pattern with about 500 thousand samples (Figure S5). Furthermore, our simulations show that for ν, the oscillations appear within less samples that for τ (Figure S6); that is, ν oscillations are apparent by averaging tens of thousands samples.
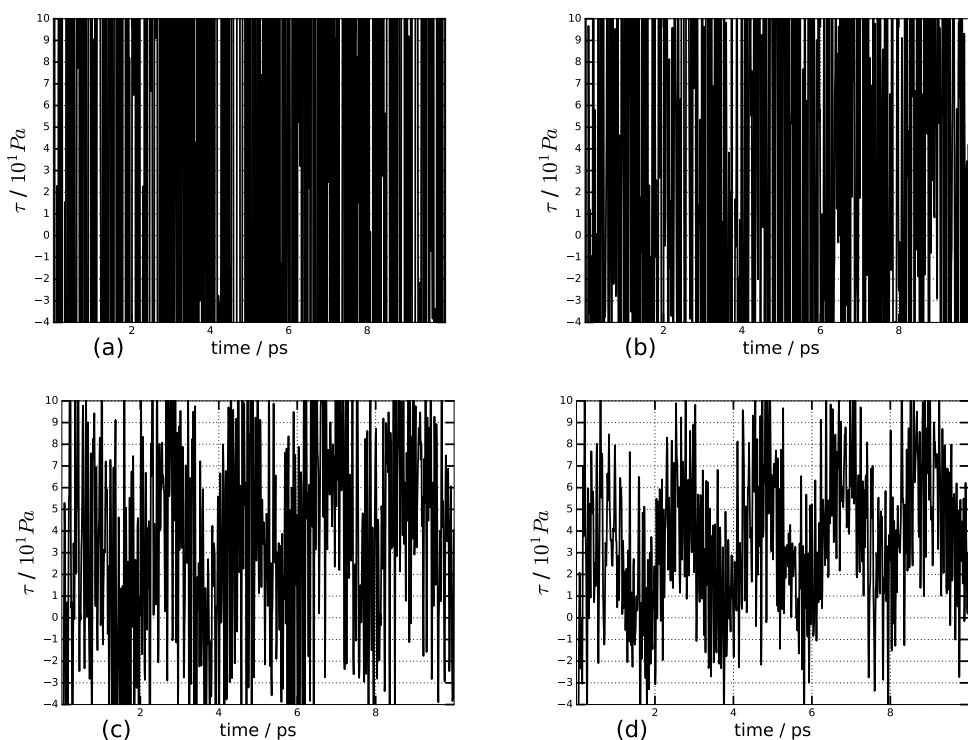
Figure S5: Sensitivity of the calculated water shear stress (τ) versus the number of samples (N). Panels show the average τ using different number of samples: (a) 800, (b) 7000, (c) 60000, and (d) 500000. τ oscillations are apparent in Panels (c) and (d).
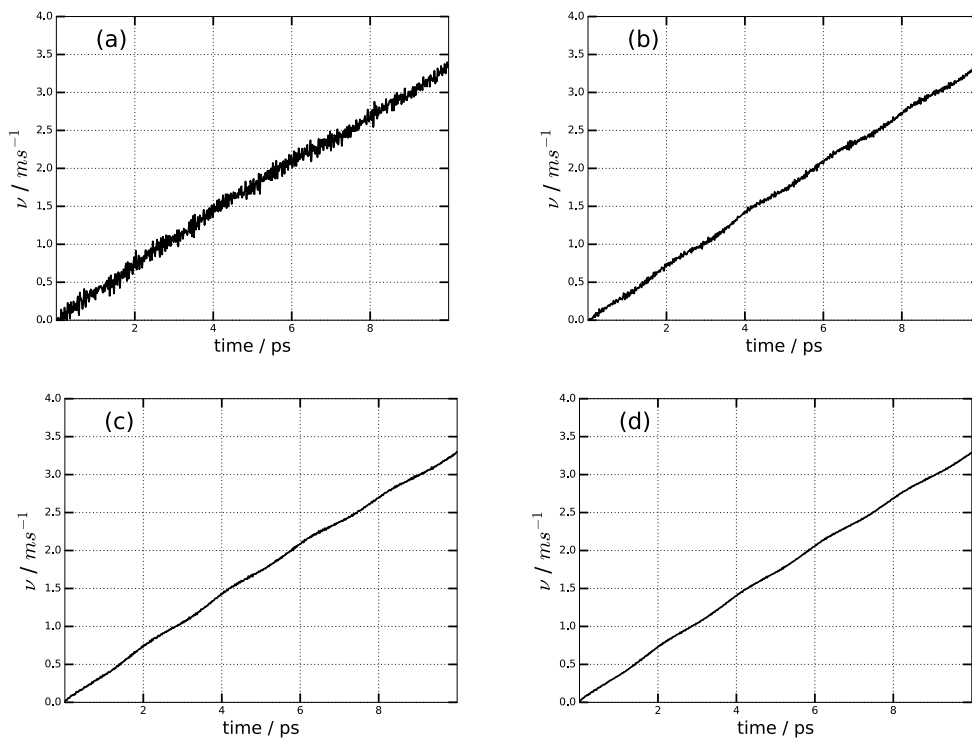
Figure S6: Sensitivity of the calculated CoM water velocity (ν) versus the number of samples (N). Panels show the average ν using different number of samples: (a) 800, (b) 7000, (c) 60000, and (d) 500000. ν oscillations are apparent in Panels (b), (c), and (d).

S4 Mean square displacements using center of mass and oxygen position

The accuracy of self-diffusion coefficient (D) relies on the slope estimation from the plot of mean square displacement (MSD) against time. Two approaches were used for calculating MSD: center of mass (MSD$_{\text{CoM}}$) and oxygen positions (MSD$_{\text{O}}$). In the following section, the plotted variable is $\frac{MSD}{2N_d}$, where N_d the dimension of the calculation, equals 1 for MSD$_{\text{CoM}}$ and 3 for MSD$_{\text{O}}$. We compare the results between MSD$_{\text{CoM}}$ and MSD$_{\text{O}}$ using two approaches of time-averaging. In the first approach [16], so-called time-shifts, we compute MSD starting from different time origins, each time origin being shifted by 0.3 ns along the trajectory. Then, all MSD curves are aligned at time zero, and averages are computed for every time, generating a mean MSD line. In the second approach [17], so-called time-windows, we split the trajectory into non-overlapping intervals of 0.3 ns, and compute MSD for each interval.
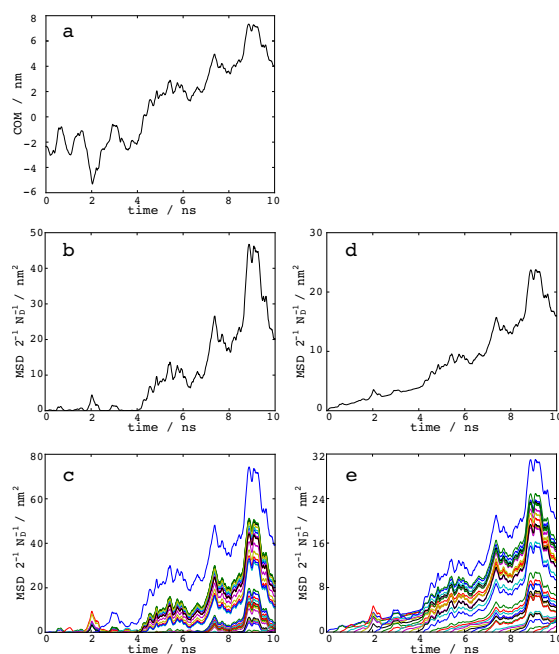
Figure S7: Computing mean squared displacements (MSD) using the time-shift averaging approach. All plots refer to a single simulation, phonon-CNT case of the inner CNT. Abscissa axis refers to MSD 2^{-1} N$_D$, where N$_D$ takes value of 1 and 3 for CoM and oxygen positions, respectively. Ordinate axis refers to time. (a) Center of mass (CoM) location of water body. (b) MSD$_{\text{CoM}}$ with reference to time zero. (c) MSD$_{\text{CoM}}$ using 0.3 ns time windows (d) MSD$_{\text{O}}$ with reference to time zero. (e) MSD$_{\text{O}}$ using 0.3 ns windows. For panels (d) and (e), each color represents one MSD curve.

Figure S7 shows the time-shift approach. This method is also used by M. Ma *et al.* to compute D from MSD_{CoM}, and it is the method used to report D in our manuscript. The CoM of water (Figure S7a) oscillates, generating a non-linear MSD_{CoM} curve (Figure S7b). Figure S7c shows MSD_{CoM} using time-shifts of 0.3 ns. The same trajectory is used to compute MSD_{O} (Figure S7d), the MSD_{O} curve improves linearity when compared to MSD_{CoM}. Finally, S7e shows MSD_{O} using time-shifts of 0.3 ns.

Figure S8 presents the procedure to obtain MSD average values from time-shift plots for one trajectory. First, the MSD curves for CoM (Figure S8a) and oxygen positions (Figure S8b) are aligned at time zero and averaged. The average over all MSD curves is smooth without fluctuations (Figure S8c). However, the value of the slope in the curve $\text{MSD} \times 2^{-1} \times N_D$ vs time is higher for MSD_{CoM} (gray line) than for MSD_{O} (black line), which will eventually lead to over/under estimations of the diffusion enhancement. For the specific trajectory presented in these plots, high CoM oscillations appear at the end (6-10 ns range, Figure S7b); thus, linearity is preserved in the first part of the trajectory. However, for other trajectories out of the 9 analyzed, high CoM oscillations appear early in the simulations, and linearity is distorted at the beginning of the trajectory (2 ns). To keep consistency among all trajectories analyzed, the D values for time-shifts were computed from the slopes of the first 1 ns.
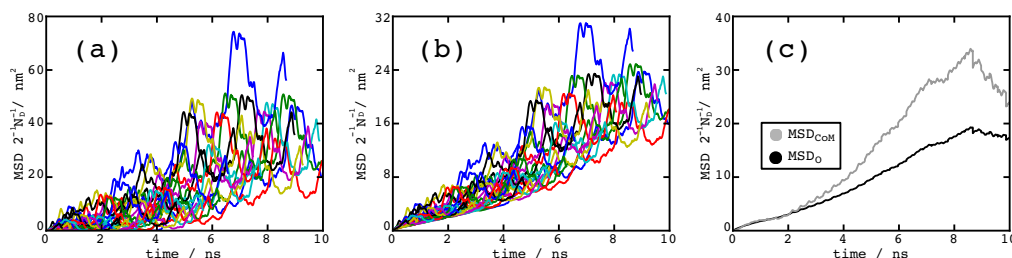
Figure S8: Averaging MSD curves from time-shifts. Panels (a) and (b) show aligned MSD curves using CoM (MSD_{CoM}) and water oxygen positions (MSD_{O}), respectively. Each color represents a MSD curve (see Figures S7c and S7e). (c) Averaged MSD for MSD_{CoM} (gray) and MSD_{O} (black).

Figure S9 shows the time-windows approach using the same trajectory. This method was initially used in our calculations, based on a publication by N. Aluru *et al.* [17], and now it is presented to show that the differences between D from MSD_{CoM} and MSD_{O} are noticeable, regardless of the procedure to compute D. Using time windows of 0.3 ns (Figure S9a), MSD_{CoM} curves improve linearity; however, linear fitting generates some slopes with negative values. Negative slopes were not considered for calculating the D average. When repeating the calculation with MSD_{O} (Figure S9d), all fitted slopes gave positive values. Noticeably, the highest diffusion is observed for the fixed CNT case; this effect is studied in section S7.

Figure S9c shows diffusion values using time-windows for different inner CNT settings. Although the diffusion values in Figure S9c are shifted in comparison to the diffusion values presented in Figure 1 in the manuscript, the overall trend persists: MSD_{CoM} estimates a higher diffusion coefficient for the phonon-active CNT case, compared to MSD_{O}, and a lower value for the phonon-free 1κ CNT case; thus, the resulting diffusion enhancement is magnified by an order of magnitude when using MSD_{CoM}. Moreover, MSD_{CoM} shows a significant dependence of the system size (Figure S9d), as it is expected that the CoM of a small body should move faster than a larger one.

11
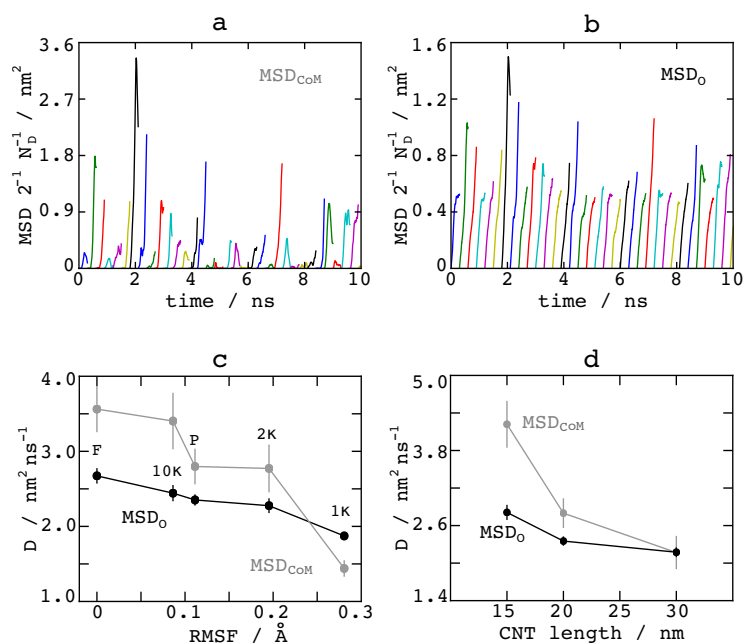
Figure S9: Computing MSD using time-windows and water self-diffusion coefficient (D). Panels (a) and (b) show MSD 2^{-1} N_D vs. time using 0.3 ns time-windows for CoM and oxygen positions, respectively. Both panels (a) and (b) refer to the same trajectory plotted in Figure S7. Panel (c) shows D values computed from MSD_{CoM} (gray) and MSD_O (black). F and P labels refer to fixed and phonon-active cases, respectively. 1κ, 2κ, and 10κ labels refer to phonon-free cases with different spring constants. CNT cases are ordered according to the root-mean-squared-fluctuations (RMSF) of the inner CNT atoms. Panel (d) compares D computed from three phonon-active CNTs of lengths 15, 20, and 30 nm. Note that D is over/under estimated when using MSD_{CoM}.

S5 Diffusion coefficient derivation

We analytically derive the Mean Square Displacement and the diffusion coefficient of CoM of water in an oscillating CNT from fluctuating hydrodynamics. In fluctuating hydrodynamics, a random fluctuating stress tensor corresponding to thermal fluctuations is introduced to the Navier-Stokes equations [18]. Thus, the CNT phonon modes are approximated as uniform oscillations. That is, our setup approximates the longitudinal modes of the CNT as a single global oscillation:

$$\boldsymbol{\nabla} \cdot \mathbf{v} = 0,$$
$$\rho \left[\frac{\partial \mathbf{v}}{\partial t} + (\mathbf{v} \cdot \boldsymbol{\nabla}) \mathbf{v} \right] = -\boldsymbol{\nabla} p + \eta \boldsymbol{\nabla}^2 \mathbf{v} + \boldsymbol{\nabla} \cdot \mathbf{S}, \tag{7}$$

where $\mathbf{S}$ is the random stress tensor which satisfies:

$$S_{ij} = S_{ji},$$
$$\langle \mathbf{S}(\mathbf{r}, t) \rangle = 0,$$
$$\langle S_{ij}(\mathbf{r}, t) S_{kl}(\mathbf{r}', t') \rangle = 2\eta kT (\delta_{ik}\delta_{jl} + \delta_{il}\delta_{jk}) \delta(\mathbf{r} - \mathbf{r}') \delta(t - t'). \tag{8}$$

We consider a cylindrical section of water of length L in an infinite carbon nanotube of radius R. The nanotube is oscillating uniformly with velocity $w = w_0 \mathrm{e}^{i\omega t}$. Thus, the CNT phonon modes are approximated as uniform oscillations; that is, our setup approximates the longitudinal modes of the CNT as a single global oscillation. We simplify the problem by assuming that the fluid flow is axial, $\mathbf{v}(\mathbf{r}, t) = v(r, t) \mathbf{e}_z$. With this assumption the problem simplifies to:

$$\frac{\partial u}{\partial t} = \frac{\eta}{\rho} \nabla_r^2 u + \zeta(r, t),$$
$$u - w_0 \mathrm{e}^{i\omega t} = -l_s \frac{\partial u}{\partial r}, \tag{9}$$

with $\nabla_r^2 = \frac{1}{r} \frac{\partial}{\partial} (r \frac{\partial}{\partial r})$ and $u(r, t) = 1/(2\pi L) \int_0^L \int_0^{2\pi} v(\mathbf{r}, t) \, \mathrm{d}\phi \, \mathrm{d}z$ is the average velocity of a shell of length L at radius r. l_S is the slip length and ζ is the thermal noise term satisfying:

$$\langle \zeta(r, t) \rangle = 0,$$
$$\langle \zeta(r, t) \zeta(r', t') \rangle = \frac{\eta kT}{\pi L \rho^2} \delta(t - t') \nabla_r \nabla_{r'} \frac{\delta(r - r')}{r'}, \tag{10}$$

where $\nabla_r = \partial/\partial r + 1/r$. Here, we have assumed that the components of the noise tensor scale like the components of the stress tensor, we thus keep only the $\nabla_r S_{zr}$ term [19, 20]. The fluid-solid interface is subject to the Navier boundary condition:

$$v - w_0 \mathrm{e}^{i\omega t} = -l_s \frac{\partial v}{\partial r}. \tag{11}$$

We begin to solve the differential equation by first homogenizing the boundary condition using the substitution: $u(r, t) = w_0 \mathrm{e}^{i\omega t} + u'(r, t)$. With this substitution, the problem translates to:

$$i\omega w_0 \mathrm{e}^{i\omega t} + \frac{\partial u'}{\partial t} = \frac{\eta}{\rho} \nabla_r^2 u' = \zeta(r, t),$$
$$u' = -l_s \frac{\partial u'}{\partial r}. \tag{12}$$

This differential equation can now be solved with the eigenfunction expansion method. We write the solution in the form of a sum of eigenfunctions:

$$u'(r,t) = \sum_{i=0}^{\infty} u_i(t) J_0(\alpha_i r). \tag{13}$$

$J_0(\alpha_i r)$ are the Bessel functions, which are derived as the eigenfunctions of:

$$\nabla_r U(r) = -\alpha_i^2 U(r). \tag{14}$$

The corresponding eigenvalues α_i are determined by the boundary condition:

$$J_0(\alpha_i R) = l_s \alpha_i J_1(\alpha_i R). \tag{15}$$

We also expand the oscillating and the noise terms into the sums of eigenfunctions:

$$i\omega w_0 = \sum_{i=1}^{\infty} b_i J_0(\alpha_i r),$$
$$b_i = \frac{2i\omega w_0}{\alpha_i R(1 + l_s^2 \alpha_i^2) J_1(\alpha_i R)}, \tag{16}$$
$$\zeta(r,t) = \sum_{i=1}^{\infty} \zeta_i(t) J_0(\alpha_i r),$$

the coefficients $\zeta_i(t)$ satisfy:

$$\langle \zeta_i(t) \rangle = 0,$$
$$\langle \zeta_m(t) \zeta_n(t') \rangle = \frac{2\eta kT \alpha_n^2 \delta_{mn} \delta(t - t')}{\pi R^2 L \rho^2 J_1^2(\alpha_n R)(1 + l_s^2 \alpha_n^2)}. \tag{17}$$

Replacing the eigenfunction expansions into equation (12), we obtain the differential equation for the $u_i(t)$ coefficients:

$$\frac{\partial u_i}{\partial t} + \frac{\eta}{\rho} \alpha_i^2 u_i = \zeta_i(t) - b_i e^{i\omega t}. \tag{18}$$

The solution of the above differential equation long after the initial conditions is:

$$u_i(t) = \frac{b_i \rho(i\omega\rho - \eta\alpha_i^2)}{\omega^2 \rho^2 + \alpha_i^4 \eta^2} e^{i\omega t} + \int_{-\infty}^{t} e^{-\eta\alpha_i^2(t-t')/\rho} \zeta_i(t') \, dt'. \tag{19}$$

Putting it all back together, we obtain:

$$u(r,t) = \left(w_0 + \sum_{i=1}^{\infty} \frac{b_i \rho(i\omega\rho - \eta\alpha_i^2)}{\omega^2 \rho^2 + \alpha_i^4 \eta^2} J_0(\alpha_i r) \right) e^{i\omega t} +$$

$$\sum_{i=1}^{\infty} J_0(\alpha_i r) \int_{-\infty}^{t} e^{-\eta\alpha_i^2(t-t')/\rho} \zeta_i(t') \, dt' \tag{20}$$

The velocity of CoM is then obtained by averaging the velocities over all shells:

$$u_{\mathrm{cm}}(t) = \frac{2}{R^2} \int_0^R u(r,t) r \, \mathrm{d}r =$$

$$w_0 \left(1 - \sum_{i=1}^{\infty} \frac{4\omega\rho(\omega\rho + \mathrm{i}\eta\alpha_i^2)}{\alpha_i^2 R^2 (\omega^2\rho^2 + \eta^2\alpha_i^4)(1 + l_s^2\alpha_i^2)} \right) \mathrm{e}^{\mathrm{i}\omega t} +$$

$$\sum_{i=1}^{\infty} \frac{2J_1(\alpha_i R)}{\alpha_i R} \int_{-\infty}^t \mathrm{e}^{-\eta\alpha_i^2(t-t')/\rho} \zeta_i(t') \, \mathrm{d}t' \quad (21)$$

The CoM displacement is now computed by integrating the CoM velocity:

$$\Delta z_{\mathrm{cm}}(t) = \int_0^t \bar{u}(t') \, \mathrm{d}t' =$$

$$w_0 \left(\frac{\mathrm{i}}{\omega} + \sum_{i=1}^{\infty} \frac{4\rho(\eta\alpha_i^2 - \mathrm{i}\omega\rho)}{\alpha_i^2 R^2 (\omega^2\rho^2 + \alpha_i^4\eta^2)(1 + l_s^2\alpha_i^2)} \right)(1 - \mathrm{e}^{\mathrm{i}\omega t}) +$$

$$\sum_{i=1}^{\infty} \frac{2J_1(\alpha_i R)}{\alpha_i R} \int_0^t \int_{-\infty}^{t'} \mathrm{e}^{-\eta\alpha_i^2(t'-t'')/\rho} \zeta_i(t'') \, \mathrm{d}t'' \, \mathrm{d}t' \quad (22)$$

It is now straightforward to obtain the mean square displacement:

$$\langle \Delta z_{\mathrm{cm}}^2(t) \rangle =$$

$$\left\{ w_0 \mathrm{Re} \left[\left(\frac{\mathrm{i}}{\omega} + \sum_{i=1}^{\infty} \frac{4\rho(\eta\alpha_i^2 - \mathrm{i}\omega\rho)}{\alpha_i^2 R^2 (\omega^2\rho^2 + \eta^2\alpha_i^4)(1 + l_s^2\alpha_i^2)} \right)(1 - \mathrm{e}^{\mathrm{i}\omega t}) \right] \right\}^2 +$$

$$\sum_{i=1}^{\infty} \frac{8k_{\mathrm{B}}T}{\alpha_i^4 R^4 \eta\pi L(1 + l_s^2\alpha_i^2)} \left[t - \frac{\rho(1 - \mathrm{e}^{-\eta\alpha_i^2 t/\rho})}{2\eta\alpha_i^2} \right] \quad (23)$$

Finally, the diffusion coefficient of CoM can now be obtained from the mean square displacement of CoM [21]:

$$D = \lim_{t\to\infty} \frac{\langle \Delta z_{\mathrm{cm}}^2(t) \rangle}{2t} = \sum_{i=1}^{\infty} \frac{4kT}{\alpha_i^4 R^4 \eta\pi L(1 + l_s^2\alpha_i^2)} = \frac{kT(1 + 4l_s/R)}{8\pi L\eta} \quad (24)$$

We show that there are two independent contributions to the mean square displacement of CoM. The first contribution is due to thermal fluctuations and for long times it results in linear mean square displacement dependence on time. The other contribution to the mean square displacement is due to the oscillating walls of the CNT. The oscillating walls introduce oscillations to the mean square displacement. Time-average of the oscillations, however, is zero. Thus, the oscillations of CNT walls do not contribute to diffusion, and the diffusion coefficient is independent of the CNT oscillations. The obtained diffusion coefficient is independent from the CNT oscillations and is in agreement with the analytical expression for the diffusion coefficient of CoM obtained by Detcheverry and Bocquet for non-oscillating CNTs [20, 22].

We observe that the derived diffusion coefficient is inversely proportional to the length of the water section L. This is also observed in our MD simulations. We also observe that the obtained diffusion coefficient corresponds to the Einstein relation between the diffusion coefficient and mobility $D = kT b$, where $b = (1 + 4L_s/R)/(8\eta\pi L)$ is the mobility [18].

In conclusion, we have shown that in the continuum description of fluctuating hydrodynamics, the oscillations of CNT walls cannot contribute to the diffusion of CoM of water. Hence, the present

mesoscale model cannot capture diffusivity enhancement for different vibrational states of the CNT. We argue that diffusion enhancement can be captured only from a finer scale model, such as Molecular Dynamics, where CNT/water friction depends on the CNT potential and state.

S6 Continuum fluid dynamics simulations
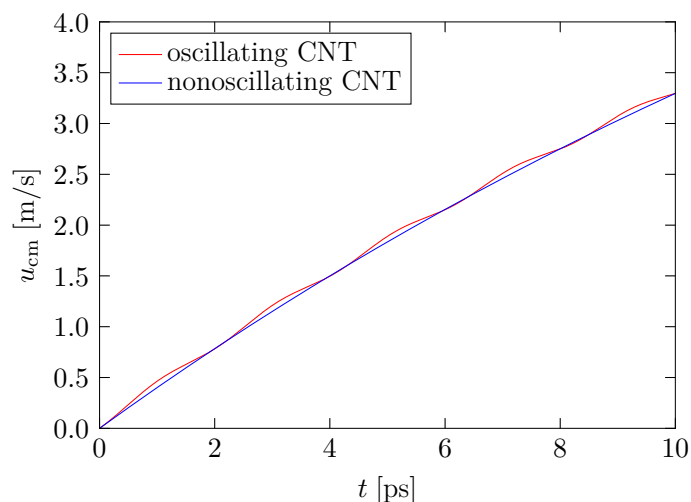
Figure S10: Velocity of CoM of water for the cases of oscillating and non-oscillating nanotubes.

We perform computational fluid dynamics simulations of water flow through nanotubes. We set up the simulation such that they correspond to the molecular dynamics simulations of Ma *et al.* [4]. We consider a nanotube of length $L = 20\,\text{nm}$ and radius $R = 1.35\,\text{nm}$. At the ends of the nanotube we apply periodic boundary conditions. The nanotube wall velocity oscillates as:

$$w(z,t) = w_0 \cos\left(\pi z/L\right) \sin\left(\omega t\right), \tag{25}$$

where $w_0 = 3.38\,\text{m/s}$ is the amplitude and $\omega = 3.05 \cdot 10^{12}\,\text{s}^{-1}$ the angular frequency. The origin of the coordinate system is placed at the center of the nanotube. The fluid inside the nanotube has density $\rho = 731\,\text{kg/m}^3$ and viscosity $\eta = 0.322\,\text{mPa}\,\text{s}$. The interface between the fluid and the nanotube is subject to the Navier boundary condition:

$$v(R,t) - w(t) = -l_s \left.\frac{\partial v}{\partial r}\right|_{r=R}, \tag{26}$$

where the slip length is $l_s = 14\,\text{nm}$. Fluid flow is induced by a pressure gradient of $\partial p/\partial z = 300\,\text{TPa/m}$. Figure S10 shows the velocity of the CoM of the bulk of water for the cases of oscillating and non-oscillating nanotubes. It is clear from the figure that the fluid velocity oscillations are very small.

Figure S11 shows the shear stress at the fluid-solid interface. We observe significant oscillations of the shear stress, even though we do not observe noticeable oscillations in the velocity.
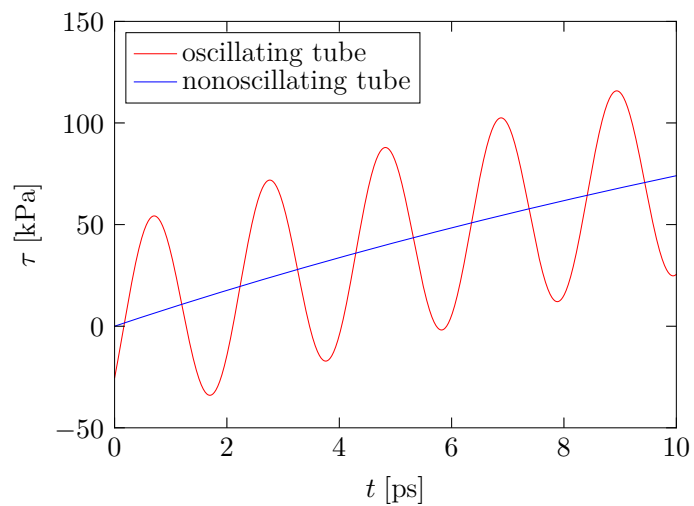
Figure S11: Shear stress on the fluid-solid interface for the cases of an oscillating and non-oscillating nanotubes.

S7   Artificial heating of water and MD parameters effects

When calculating diffusion for different CNT cases (phonon-active, phonon-free and fixed CNT) using time-windows (section S4), the highest D value is obtained for the fixed CNT. These simulations are carried out for more than 10 ns. Although it is expected that a well-equilibrated system should keep a constant temperature level, and energy shift should remain negligible, we observe for fixed CNT-cases an artificial increment of the water temperature from initial 297.60 ± 2.56 K to 306.08 ± 3.79 K at the end of 10 ns, while phonon-active and phonon-free CNT-cases remain at a stable temperature. For phonon-active and phonon-free CNT-cases, the inner CNT is thermostated; thus, mobile CNT atoms are able to extract energy from the water and, thus, dissipate water heating. Figure S12 shows the water temperature variation with time for phonon-active and phonon-free 1κ cases; while the inset figure shows the temperature of CNT mobile atoms. For both phonon-active and phonon-free cases, the inner CNT remains at 298K; and water is effectively thermalized by mobile CNT atoms, counterbalancing water heating.
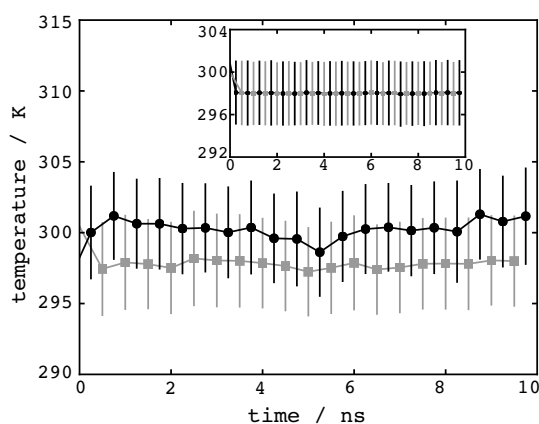
Figure S12: Temperature for water and carbon for phonon-free (gray squares) and phonon (black circles). Note that, although phonon CNTs thermalize water and counterbalance numerical heating, they still keep the temperature of water about 2-3 degrees higher than that of CNT. Inset shows temperature of inner CNT atoms.

It is worth noting that in the phonon-active CNT-case (Figure S12- black circles), the water temperature remains 2-3 K higher than in the phonon-free case (Figure S12- gray squares). The different thermalizing effect of phonon-active and phonon-free cases is quantified by calculating thermal contact conductance (h_c) at the water-carbon interface.

We compute h_c with simulations of the Heat Transfer group. The MD protocol for this group was introduced in Section S1. In the following lines, we provide further details for Heat Transfer simulations and the calculation of thermal conductance h_c. Starting from fully equilibrated systems, we applied force equal to 0.012 pN to water molecules, and carried out Heat Transfer simulations up to reaching a stable temperature. For all CNT cases, water temperature reaches equilibrium state after 5 ns. After that, we continued the simulations for 3 ns (Figure S13a), recording water temperature, inner-CNT temperature, and heat added to the inner-CNT from the thermostat. The output values are used to compute h_c from:

$$h_c = \frac{q}{A \, \Delta T},\tag{27}$$

where A the interface area; q and ΔT are the heat exchange and temperature difference at the water-CNT interface, respectively. To compute the temperature difference between water and carbon at the interface (ΔT), we first compute the radial temperature profile of water. Then, we apply linear regression to obtain the temperature of the outermost water layer in contact with the inner-CNT. ΔT was computed by subtracting the outermost water temperature and the inner CNT temperature. To establish a relation between inner-CNT mobility and thermal conductance, we computed the root-mean-square-fluctuations (RMSF) of the inner-CNT atoms using the MD-Analysis tool [23]. Figures S13b and S13c show the variation of ΔT and q against RMSF.
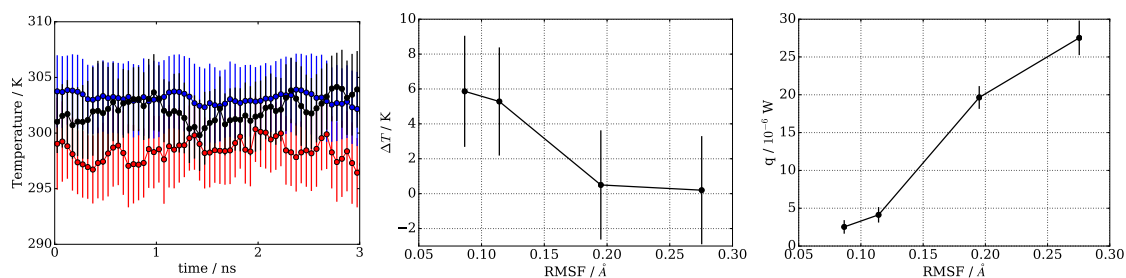
Figure S13: Thermal contact conductance calculation. (a) Time evolution of temperature for water molecules after reaching steady state. Curves refer to Heat Transfer group simulations. The lines are averages for phonon-active (black), phonon-free-1κ (red), and phonon-free-10κ (blue). (b) Temperature difference between the last radial rank of water atoms and inner CNT atoms vs RMSF of inner CNT. (c) Heat transferred to the thermostated inner-CNT vs RMSF of inner CNT.

Finally, we relate the extend of heat dissipation to the mobility of carbon atoms: the higher the RMSF of CNT, the higher the thermal conductance h_c (Figure S14); thus, mobile CNTs can effectively dissipate the artificial heating of water.
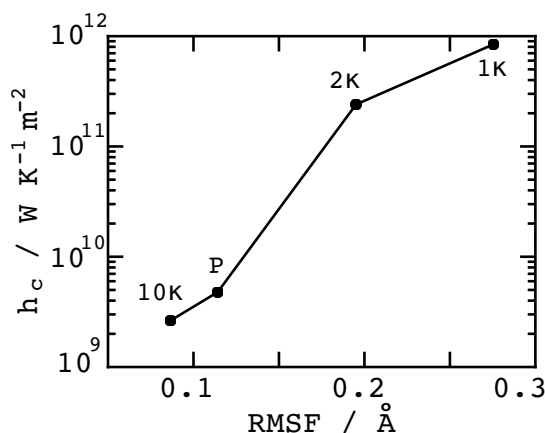
Figure S14: Thermal contact conductance (h_c) at the water-CNT interface for different CNT-cases. h_c is not calculated for fixed CNT-case, as the CNT temperature is 0 K.

As a next step, we try to identify the source of heating by varying different MD protocol parameters. We repeat the simulation of a fixed CNT, in which the artificial heating is present, while varying MD parameters. Figure S15 shows the temperature variation when changing shake tolerance, time step, cutoff, and long-range electrostatics tolerance. Water temperature is sensitive to all MD protocol parameters, with long-range electrostatics, calculated through particle-particle particle-mesh (P3M) method, affecting it the most.
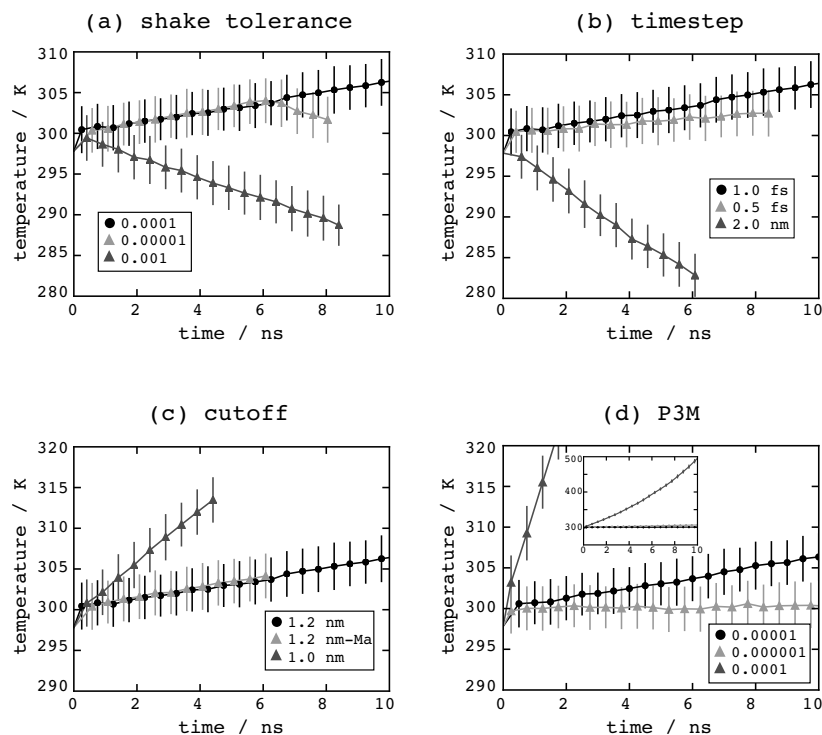
Figure S15: Effect of MD protocol options on water temperature. Plots show water temperature inside a fixed CNT using different MD protocol parameters. (a) Effect of shake tolerance on water temperature using shake tolerance values of 10^{-4} (black circles), 10^{-3} (dark gray triangles), and 10^{-5} (gray triangles). Note that the finer shake tolerance of 10^{-5} produces a decrease in temperature after 6 ns. (b) Effect of timestep on water temperature using timestep values of 1.0 fs (black circles), 0.5 fs (gray triangles), and 2 fs (dark gray triangles). (c) Effect of cutoff for short range interactions using two different cutoff values of 1.2 nm (black squares) and 1.0 nm (dark gray triangles), with skin value of 2.5 Å and list update every 1 timestep. A setup similar to Ma *et al.* [4] (gray triangles), considers a cutoff of 1.2 nm, skin value of 2.0 Å and update list every 5 timesteps. (d) Effect of the P3M long-range electrostatic on water temperature with different RMSE values of 10^{-4} (black circles), 10^{-5} (gray triangles), and 10^{-6} (dark gray triangles). Inset shows a zoom-out view. Black circles in panels (a-d) refer to the same MD simulation.

In the case of P3M, we note that the standard root-mean-square error (RMSE) for P3M using TIP4P-Ew is 10^{-5}; such RMS tolerance still results in artificial heating of water in fixed CNTs [24]. Figure S16 shows the extend that RMSE parameter affects the force calculation.
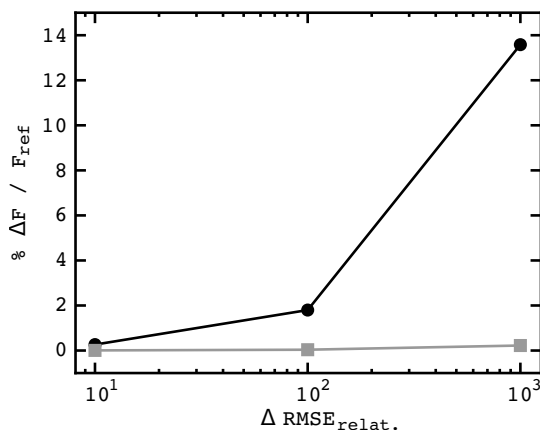
Figure S16: Effect of long-range electrostatic parameters on force calculation. The figure shows how increments in root-mean-square-error (RMSE) parameter from particle-particle particle-mesh (P3M) affect force calculation. Forces are compared relative to a reference RMSE of 10^{-6}. X-axis shows the relative RMSE; note that logarithmic scale is applied. Y-axis shows force variation ($\%\Delta F$). Black circles refer to water molecules inside a fixed CNT. Gray squares refer to a bulk water box, periodic in all directions.

The relative RMSE is calculated from:

$$\mathrm{RMSE_{relat.}} = \frac{\mathrm{RMSE_{mod}}}{\mathrm{RMSE_{ref}}},$$

where $\mathrm{RMSE_{mod}}$ are RMSE values of 10^{-5}, 10^{-4}, and 10^{-3}, and $\mathrm{RMSE_{ref}}$ is 10^{-6}. Y-axis shows the percentage of force variation:

$$\%\Delta F = \frac{F_{mod} - F_{ref}}{F_{ref}} \times 100,$$

where F_{mod} and F_{ref} are forces acting on water-oxygen atoms using $\mathrm{RMSE_{mod}}$ and $\mathrm{RMSE_{ref}}$, respectively. Forces were obtained by recomputing (LAMMPS RERUN option) 10 ns NVE equilibrations. Only the RMSE parameter was changed when recomputing forces (LAMMPS KSPACE_STYLE PPPM/TIP4P option).

In Figure S16, black circles correspond to a simulation of a fixed CNT filled with water and gray squares to a periodic water box of 4 nm length. Fixed-CNT systems prove to be highly affected by increment of the force on water oxygens, which is in agreement with increase of water temperature. Conversely, a compact periodic 3D water box shows high tolerance to RMSE variation.

S8   Friction coefficient

To calculate the friction coefficient (λ), we followed the procedures described by Falk *et al.* [25]. First, we computed the force time correlation function, so-called FACF:

$$FACF(t) = \langle F(t) \cdot F(0) \rangle, \tag{28}$$

where F(t) is the total axial force between water and CNTs at time t. Then, λ is obtained from the integral of FACF as follows:

$$\lambda = \frac{1}{Ak_BT} \int_0^\infty FACF(t)dt, \tag{29}$$

where k_B is the Boltzmann constant, T is 298 K, and A is the area of the inner CNT. A numerical artifact of this calculation is that the integral of FACF tends to zero for very long times [26]. This problem is circumvented by identifying a plateau in λ before decay starts; for CNTs of a similar radius, such plateau is observable between 0.6 to 2 ps [25].

Figures S17a and S17b show FACF(t) and its integral, respectively. As mentioned in Section S1, Friction group simulations are used for the estimation of the friction coefficient λ. For each CNT case, five independent 500-ps simulations are performed. Thus, each curve in Figures S17 represents an average of (5 systems×500 ps/2 ps) = 1250 curves. A first observation is that FACF is highly correlated for phonon-free systems (red, purple and cyan curves in Figure S17a). This is because CNTs are positionally restrained with a harmonic oscillator, mimicking a spring. The high correlation for phonon-free CNTs is propagated into the integral calculation (Figure S17b). Since oscillations appear up to 1.5 ps, we shorten the range for λ averaging; instead of using from 0.6 to 2.0 ps, we only considered the range from 1.6 to 2.0 ps.
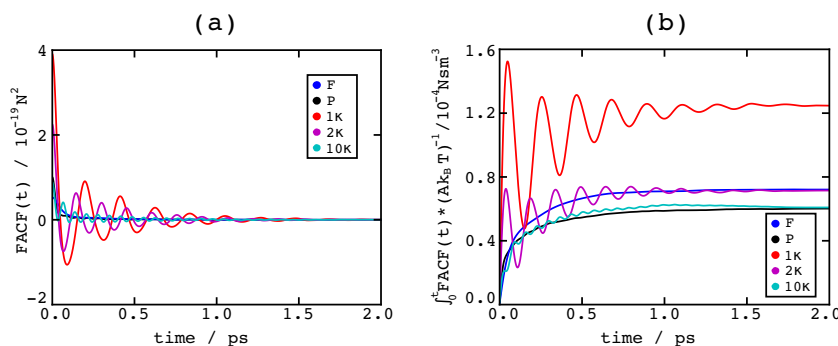
Figure S17: Friction coefficient calculation for CNTs. Panel (a) shows the time correlation function for axial force between water and CNTs. Panel (b) shows the integral of FACF; values are normalized by Ak_BT (Equation 29). Labels F, P, 1κ, 2κ and 10κ refer to fixed (blue), phonon-active (black), phonon-free-1κ (red), phonon-free-2κ (purple), phonon-free-10κ (cyan) CNTs, respectively.

The effect of surface friction on water flow can be quantified by the slip-length [27] : $L_s = \frac{\eta}{\lambda}$, where η the shear viscosity ($\eta = \frac{k_BT}{3\pi\alpha}\frac{1}{D}$), with α being the average molecular diameter of water (0.17 nm) [27]. Phonon-free 1κ CNT has the smallest slip-length (Figure S18); thus, the specific CNT settings for phonon-free 1κ significantly slow down water diffusion.
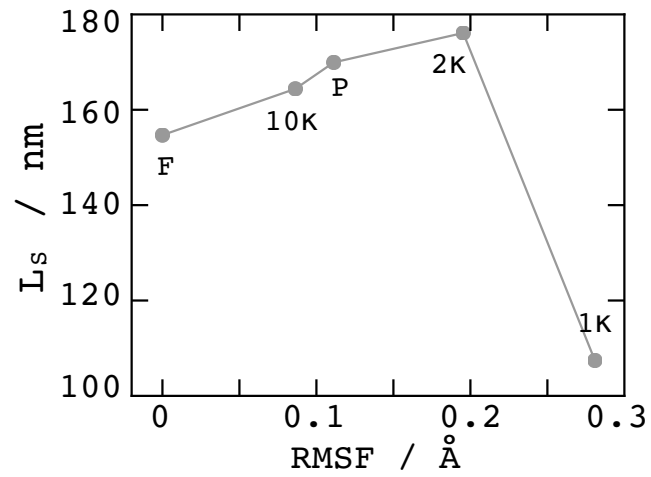
Figure S18: Slip length (L_S) of CNTs. Abscissa axis shows RMSF of the inner CNT atoms. F and P labels refer to fixed and phonon-active cases, respectively. 1κ, 2κ, and 10κ labels refer to phonon-free cases with different spring constants.

S9   Open CNT systems

Regardless of the choice of either MSD_{CoM} or MSD_O, diffusion values can only loosely connect the effect of an oscillating CNT with water flow. To solve this issue, we carry out a final set of MD simulations using a setup so-called "Open System" of water and CNTs. The systems consider inlet and outlet reservoirs, whereas a pressure gradient is applied through a moving piston (Figure S19a). Such a setup allows us to directly quantify water flow (Q) under pressure, while including CNT vibration effects. The Open System setup has already been used to simulate water flow in CNTs of lengths close to experimental devices [28]. We must highlight that in the Open Systems, the CNTs are not periodic and the observable is Q, whereas in the cases presented in the main manuscript, the CNTs are periodic and the observable is D. Figure S19b shows a 20 % enhancement for Q in phonon-active over phonon-free 1κ CNTs; once more the latter CNT has the lowest flow rate.

Building open CNT systems

CNT open systems consist of two water boxes, termed as inlet and outlet reservoirs, of $10\times10\times9$ nm^3 and $10\times10\times2.5$ nm^3, respectively (see Figure S19a). Water boxes are created with the plugin `Solvate` in VMD [9]. The water reservoirs are connected through a DWNT with chiral indexes of (20,20) and (25,25), and axial length of 20 nm (green beads in Figure S19a). DWNT is filled with water (red and white beads in Figure S19a) from a previous solvation step (section S1). In each reservoir, a graphene layer, so-called border (blue beads in Figure S19a), is placed near the CNT opening, which allows water flow only through the CNT channel. In the inlet, an extra graphene layer, so-called piston, is located on top of the water (purple in Figure S19a). The systems are periodic, with unit cells of $10\times10\times42.6$ nm^3, providing 10 nm distance of empty space between periodic images of the piston and the outlet reservoir.

MD setup and equilibration

For border and piston CNT atoms, bonding terms are considered (bond, angles, dihedrals). For the inner CNT atoms, four different settings are used: fixed, phonon-active, 1κ phonon-free, and 10κ phonon-free. Outer CNT atoms are fixed. Border atoms are positionally restrained using harmonic constrained with a spring constant of 230.6 kcal mol^{-1}Å^{-2} (10κ). Piston atoms are also restrained using a 10κ spring constant , but only in the X- and Y- axes; thus, the piston is free to move in the Z-axis. Force field potentials and MD protocol options are the same as the ones described in section S1.

For equilibration, four separate thermostat controls at 298K are applied on the border, inner CNT, piston, and water. Four systems are equilibrated: fixed, phonon-active, 1κ phonon-free, and 10κ phonon-free. The MD equilibrations are carried out for 7 ns in NVT conditions.

Production runs

After equilibration, the thermostat controls in the piston layer and water are removed; whereas thermostats are kept for the inner CNT and barriers. A constant force of 0.52 pN is applied to each piston atoms, which generates a pressure of 200 bar in the inlet. Such high pressure is needed to generate a significant flow within dozen of nanoseconds.

The systems are simulated for about 13-15 ns. The flow is measured by counting the number of water molecules in the outlet reservoir over time. Consecutive 1-ns intervals are used to measure flow; that is, the values in Figure S19b are averages and standard errors over 12-14 measurements. The first nanosecond is not considered.
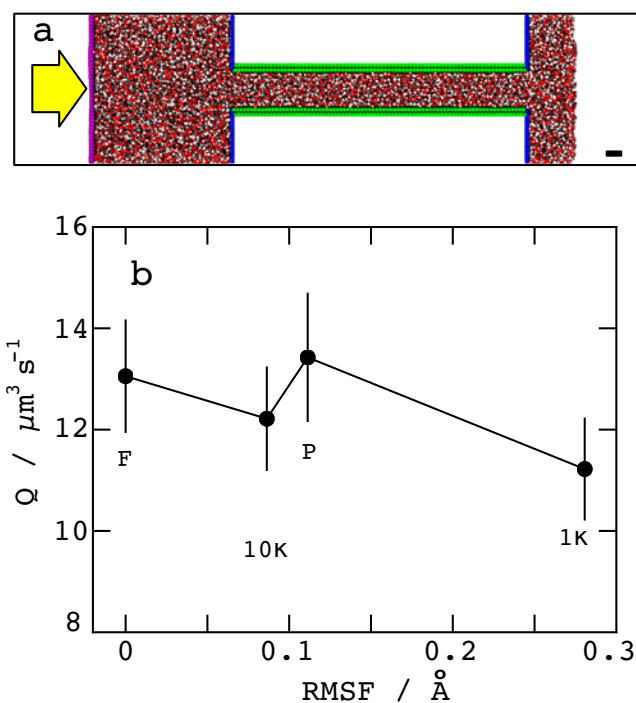
Figure S19: Water transport through vibrating open CNTs. Figure (a) shows an all-atom MD model of CNT filled with water with inlet (left) and outlet (right) compartments. Water molecules are pictured as red and white beads, CNT atoms are represented in green. Inner and outer CNTs have [n,m] chiralities of (20,20) and (25,25), respectively. Reservoir barriers are shown in blue. An axial force is applied to a piston layer (purple) to generate a pressure gradient that drives water from the inlet to the outlet compartments (see SI). Scale bar at the bottom right is 1 nm. Panel (b) shows volumetric flow rates (Q) under 200 bar pressure. F and P labels refer to fixed and phonon-active cases, respectively. 1κ and 10κ labels refer to phonon-free cases with different spring constants (see SI). CNT cases are ordered according to the root-mean-square-fluctuations (RMSF) of the inner CNT atoms.

S10   Movie of CNT permeation

M1.mov shows permeation of a DWNT during 1 ns NPT simulations (see Methods section described above).

References

[1] S. Plimpton. Fast parallel algorithms for short-range molecular dynamics. *J. Comput. Phys.*, 117:1–19, 1995.

[2] H. W. Horn, W. C. Swope, J. W. Pitera, J. D. Madura, T .J. Dick, G. L. Hura, and T. Head-Gordon. Development of an improved four-site water model for biomolecular simulations: TIP4P-Ew. *J. Chem. Phys.*, 120:9665–9678, 2004.

[3] V. Kräutler, W. F. Van Gunsteren, and P. H. Hünenberger. A fast SHAKE algorithm to solvedistance constraint equations forsmall molecules in moleculardynamics simulations. *J. Comput. Chem.*, 22:501–508, 2001.

[4] M. Ma, F. Grey, L. Shen, M. Urbakh, S. Wu, J. Z. Liu, Y. Liu, and Q. Zheng. Water transport inside carbon nanotubes mediated by phonon-induced oscillating friction. *Nat. Nanotechnol.*, 10:1–5, 2015.

[5] S. L. Mayo, B. D. Olafson, and W. A. Goddard. DREIDING: A generic force field for molecular simulations. *J. Phys. Chem.*, 94:8897–8909, 1990.

[6] M. Deserno and C. Holm. How to mesh up Ewald sums. I. a theoretical and numerical comparison of various particle mesh routines. *J. Chem. Phys.*, 109:7678–7693, 1998.

[7] D. Frenkel and B. Smit. *Understanding Molecular Simulation.* 2002.

[8] WCCNT. https://github.com/cselab/wccnt.

[9] W. Humphrey, A. Dalke, and K. Schulten. VMD – Visual Molecular Dynamics. *J. Mol. Graphics.*, 14:33–38, 1996.

[10] M. Shirts and V.S. Pande. COMPUTING: Screen savers of the world unite. *Science*, 290:1903–1904, 2000.

[11] P. Angelikopoulos, C. Papadimitriou, and P. Koumoutsakos. Bayesian uncertainty quantification and propagation in molecular dynamics simulations: A high performance computing framework. *J. Chem. Phys.*, 137:144103, 2012.

[12] P. Angelikopoulos, C. Papadimitriou, and P. Koumoutsakos. Data driven, predictive molecular dynamics for nanoscale flow simulations under uncertainty. *J. Phys. Chem. B.*, 117:14808–14816, 2013.

[13] S. Wu, P. Angelikopoulos, C. Papadimitriou, R. Moser, and P. Koumoutsakos. A hierarchical bayesian framework for force field selection in molecular dynamics simulations. *Philos. T. R. Soc. A*, 374:20150032, 2015.

[14] P. E. Hadjidoukas, P. Angelikopoulos, C. Papadimitriou, and P. Koumoutsakos. π4u: A high performance computing framework for bayesian uncertainty quantification of complex models. *J. Comput. Phys.*, 284:1–21, 2015.

[15] M. D. Ma, L. Shen, J. Sheridan, J. Z. Liu, C. Chen, and Q. Zheng. Friction of water slipping in carbon nanotubes. *Phys. Rev. E.*, 83:036316, 2011.

[16] G. Pranami and M. H. Lamm. Estimating error in diffusion coefficient derived from molecular dynamics simulations. *J. Chem. Theory. Comput.*, 11:4586–4592, 2015.

[17] A. Barati Farimani and N.R. Aluru. Spatial diffusion of water in carbon nanotubes: From fickian to ballistic motion. *J. Phys. Chem. B.*, 115:12145–12149, 2011.

[18] L. D. Landau and E. M. Lifshitz. *Fluid Mechanics*, volume 6 of *Course of Theoretical Physics*. Pergamon Press, Oxford, 1959.

[19] Günther Grün, Klaus Mecke, and Markus Rauscher. Thin-Film Flow Influenced by Thermal Noise. *J Stat Phys*, 122(6):1261–1291, 2006.

[20] François Detcheverry and Lydéric Bocquet. Thermal fluctuations of hydrodynamic flows in nanochannels. *Phys. Rev. E*, 88(1):012106, 2013.

[21] Ian N. Sneddon. On some infinite series involving the zeros of Bessel functions of the first kind. *Glasgow Math. J.*, 4(3):144–156, 1960.

[22] François Detcheverry and Lydéric Bocquet. Thermal Fluctuations in Nanofluidic Transport. *Phys. Rev. Lett.*, 109(2):024501, 2012.

[23] N. Michaud-Agrawal, E. J. Denning, T. B. Woolf, and O. Beckstein. MDAnalysis: A toolkit for the analysis of molecular dynamics simulations. *J. Comput. Chem.*, 32:2319–2327, 2011.

[24] M. Ma *et al.* stated a RMS error of 10^{-4} for his calculations (Supp. Inf. in his manuscript); however, their production run simulations were carried out with a RMS error of 10^{-5} (personal communication).

[25] K. Falk, F. Sedlmeier, L. Joly, R. R. Netz, and L. Bocquet. Molecular origin of fast water transport in carbon nanotube membranes: Superlubricity versus curvature dependent friction. *Nano Lett.*, 10:4067–4073, 2010.

[26] L. Bocquet and J. L. Barrat. On the green-kubo relationship for the liquid-solid friction coefficient. *J. Chem. Phys.*, 139:044704, 2013.

[27] J.A. Thomas and A. J. H. Mcgaughey. Reassessing Fast Water Transport Through Carbon Nanotubes. *Nano Lett.*, 8:2788–2793, 2008.

[28] Walther J. H., K. Ritos, E. R. Cruz-Chu, C. M. Megaridis, and P. Koumoutsakos. Barriers to Superfast Water Transport in Carbon Nanotube Membranes. *Nano Lett.*, 13:1910–1914, 2013.